**Library Progress International** *Print version ISSN 0970 1052*
*Vol.44 No. 3, Jul-Dec 2024: P. 17174-17188* *Online version ISSN 2320 317X*

*Original Article* *Available online at www.bpasjournals.com*

# Detection of Ovarian Cancer with optimized Neural Networks using Convolutional LSTM

**[1]Namani Deepika Rani, [2]Dr.Mahesh Babu Arrama**

[1]Research Scholar, CSE Department, Koneru Lakshmaiah Education Foundation, Hyderabad, India
[2]Professor, CSE Department, Koneru Lakshmaiah Education Foundation, Hyderabad, India

**How to cite this article:** Namani Deepika Rani, Mahesh Babu Arrama (2024) Detection of Ovarian Cancer with optimized Neural Networks using Convolutional LSTM. *Library Progress International,* 44(3), 17174-17188

**Abstract:** Ovarian cancer ranks as the sixth deadliest cancer in the United States, underscoring the urgent need for a non-surgical diagnostic assay with both high sensitivity and specificity. Such a breakthrough would greatly accelerate treatment and enhance the quality of life for affected individuals. In this research, an automated framework was created using optical coherence tomography (OCT) recordings to look for signs of ovarian cancer in transgenic mice. This study was carried out to aid in the remedying of this problem. In order to evaluate temporally ordered sequences of optical coherence tomography (OCT) tomograms, this advanced approach employs neural networks. Three distinct neural network-based strategies were employed, including a VGG-supported feed-forward network, a 3D convolutional neural network, and a convolutional LSTM (Long Short-Term Memory) network. Regarding the noise that is present in all OCT images, the results show that these models achieve high performance with no adjusting or feature creation needed. What a surprising discovery. The best model is a convolutional LSTM-based neural network, with a mean area under the curve (± standard error) of 0.86 ± 0.052. To our knowledge, no previous literature documents the use of machine learning to interpret depth-resolved OCT images of entire ovaries, hence this study represents an important first step in this direction. As a result, this study stands out as an innovative one. This diagnostic technique has enormous prospects for early identification and intervention in the case of this extremely deadly condition since it has the potential to be transferred from transgenic mice to human tissue. Transgenic mice are currently used as the only diagnostic tool for this disease.
**Keywords:** Convolutional neural networks, Deep learning, Optical coherence tomography, LSTM (Long Short-Term Memory), Ovarian cancer.

## 1. INTRODUCTION

There has been a noticeable rise in both the incidence of cancer and the prevalence of cancer diagnoses during the previous 15 years. Thus, cancer has become the second leading cause of mortality in the USA, after heart disease. In the United States, ovarian cancer is now the sixth leading cause of cancer-related death [1]. Cancer comes in various forms; ovarian cancer is one of them. Ovarian cancers non-specific symptoms, many of which, taken individually, don't seem serious, are a major factor in the disease's lethality. A frightening 80% of diagnoses are made too late [2] due to a lack of specific symptoms and the absence of an efficient early screening device. This is because there is currently no reliable method of early screening. However, there is some good news: the five-year survival rate for ovarian cancer soars to 94% when it is detected and treated before it has spread [2], compared to a baseline survival rate of 28% for those diagnosed at the metastatic stage. This compelling data underscores the critical necessity for an efficient and reliable early detection technique for ovarian cancer.

Screening for ovarian cancer that does not involve surgery and has a high throughput has great promise for enhancing patients' quality of life and survival rates. Diverse imaging techniques have been explored in the pursuit of this goal, with optical coherence tomography (OCT) showing particularly encouraging results. Optical coherence tomography (OCT) is an interferometric imaging technique that has gained popularity for its depth-resolved, high-resolution pictures. These pictures convey crucial details about the microstructure of the examined tissue. Optical coherence tomography has a long history of success in the field of biological imaging, especially in the human eye [3-5], lung [6, 7], esophagus [8], coronary artery [9, 10], and other organs, including the ovaries [11-13]. To begin with, OCT devices measure time-resolved backscattered light rather than sound waves [14], which is where they diverge most from ultrasound. Similar to the idea that supports ultrasonic technology, OCT devices are based on a fundamental principle. In particular, OCT images reveal

a lot of micro structural information on the ovary. The stroma, epithelium, and collagen are examples of such finer points, and they hold great potential for disease diagnosis and tissue classification [11, 12, 15–18].

Optical coherence tomography (OCT) presents a number of challenges when used for the screening of ovarian cancer [19]. One such challenge is optical noise, which is present in all tomographic imaging of the ovaries. Moreover, OCT data is acquired in a three-dimensional format, which may lead to scaling issues and depth-dependent imaging performance. The existence of these factors, along with the speckle noise that is characteristic of the imaging, makes it exceedingly difficult for human radiologists and oncologists to establish reliable diagnoses. It is for this reason that the application of cutting-edge computational technologies, most notably machine learning strategies, is gaining traction for the extraction of quantitative diagnostic information for the aim of cancer screening.

The goal of the paper is to examine recent categorization methods based on neural networks in an effort to solve this issue. The results are very promising and may indicate that machine learning can detect early tissue abnormalities related with the development of cancer. Research shows that deep VGG-like 3D convolutional neural networks, when combined with convolutional LSTMs (Long Short-Term Memory; similar in design to those previously employed), can achieve remarkable diagnostic accuracy. These analyses made use of a dataset containing optical coherence tomography (OCT) recordings of mouse ovaries, acquired in a mouse model developed to mimic the development of ovarian cancer [20, 21].

In this section, we establish the variables, parameters, and general notation that will be consistently used throughout this research. Firstly, we introduce the concept of a sample, denoted as $X_t$. A sample Xt represents a sequence of OCT (optical coherence tomography) images and can be expressed as $X_t = [x_{t,1}, ..., x_{t,j}, ..., x_{t,N}]$, where 't' serves as an index referring to a specific animal sample, 'N' stands for the number of slices within a sequence, and $x_{t,j}$ corresponds to the $j^{th}$ image within this sequence, associated with the animal indexed by 't'. Notably, this sequence of images is formed by concatenating subsequences of tomograms obtained from both the left and right ovaries. To illustrate, if we assume N = 50, then each $X_t$ comprises 50 sequential images, with 25 images originating from each ovary. These images progress from the most superficial to the deepest slices.

Furthermore, each animal in the study is assigned a label, represented by the symbol $y_t$, which can take on values between zero and one. If $y_t = 1$, then animal t is transgenic and is more likely to develop ovarian cancer by the age of 8 weeks, but if $y_t = 0$, then the mice are of the wild-type (WT) variety. The following are examples of how the neural network predicted these labels: D: = $\{X_t, y_t\}$ for t = 1 to T, where T is the total number of samples or animals in the study, is the notation we'll use throughout this examination to refer to a dataset as a collection of tuples.

The structure of this manuscript can be found in the following outline: The terminology used in the rest of the text is established and defined in Section 2. This will help us communicate effectively. Optical coherence tomography (OCT) and neural networks have shown promise in the detection of ovarian cancer, and in this section we provide a brief overview of the relevant research and development in this area. Information on how the OCT data from the ovarian tissue samples were collected and prepared for analysis is provided in this section. The methods for gathering the data are discussed in detail here. In this section, we go over our data preprocessing method, describing in detail the steps we take to get the OCT data ready to be fed into our neural network models. Getting the OCT data ready to feed into our neural network models is the focus of Section 4.3. We have reached the end of section 4. Several different types of neural networks were explored in this study; their designs and configurations are described in detail in Section 3.4 below. Section 4: Section 4 serves as the core of our evaluation, where we present a thorough assessment of the diagnostic efficacy of the neural networks we employed. This section includes detailed analysis and results. Section 5: Finally, in Section 5, we offer interpretation and discussion of the results presented in Section 5, providing insights into the implications and potential advancements in ovarian cancer detection using OCT and neural networks.

## 2. RELATED WORK

Optical coherence tomography (OCT) stands as a valuable resource for gathering extensive information about tissue health. However, there are many challenges involved in quantitatively analyzing ovarian OCT data collected in three dimensions. Many factors, including the data's high dimensionality, its depth dependence, the presence of speckle noise, and the substantial biological variety intrinsic to ovarian tissue, contribute to these problems. First- and second-order statistical techniques, including as texture analysis, shape analysis, and frequency analysis [22, 23], have been the mainstay of quantitative studies of whole ovarian OCT images till now. Although these strategies, which make use of OCT imaging technology, have shown promise in evaluating tissue abnormalities associated with various cancers, there is still a lot of room for considerable improvement in both sensitivity and specificity. A more precise and accurate detection of ovarian cancer is possible through the implementation of advanced machine learning methods.

Ovarian cancer detection studies that employ optical coherence tomography (OCT) and convolutional neural networks (CNNs) are gaining traction. While studies up to my last knowledge update in September 2021 were relatively limited, they demonstrated promising potential. These investigations primarily focused on developing machine learning algorithms, particularly CNNs, to analyze OCT images of ovarian tissue for early cancer detection. Some studies aimed to distinguish between healthy and cancerous ovarian tissues by leveraging the distinctive features visible in OCT images. OCT data complexity, depth dependency, speckle noise, and biological variability inside the ovaries were all challenges that needed to be overcome. Although this field was in its early stages, the results indicated that machine learning techniques, including CNNs, had the capacity to enhance the accuracy and efficiency of ovarian cancer diagnosis through OCT imaging [24]. Given the dynamic nature of scientific research, it is advisable to explore recent literature and academic sources for the latest advancements in this field beyond my last update.

Neural networks and related technologies have demonstrated promising results in the field of optical coherence tomography (OCT) biological imaging. Machine learning has shown useful in several fields, including the identification of ocular diseases like glaucoma [25, 26], retinal diseases such macular degeneration [27-30], cancers including lung [20], and neurological and dermatological diseases like lupus [31, 32]. There have also been significant developments in the application of machine learning to intravascular OCT imaging. Successful applications of techniques like neural networks and random forests have been made to detect atherosclerotic plaques [33–35]. Because of this, machine learning has been able to make great strides in recent years. The use of pulmonary X-ray imaging for the detection of COVID-19 has also been proven using neural networks [36].

The progress made in other areas of cancer diagnosis using machine learning indicates that there is a realistic route for the development of the technology in the context of ovarian tissue imaging, which could lead to therapeutic applications. It is to the best of our knowledge the first time that deep neural networks have been utilized to interpret whole-ovary depth-resolved OCT images. It is worth noting that this is the case, as it is an essential point to transmit.

The machine learning community at large agrees that transfer learning is a valuable technique [37, 38]. During transfer learning, a model (such as a neural network) is trained on a task that may or may not have a strong relationship to the task on which it will be evaluated. This assessment is scheduled for the future. For instance, identifying cancer is not the same task as designing a neural network to classify ImageNet data [39]. A neural network trained on ImageNet, however, might have picked up some helpful properties from actual images. If the network is trained on ImageNet, these features can be used to classify OCT images for malignancy. One of the tactics we employ in this inquiry to enhance the general performance of our prediction model is transfer learning, which has proven to be quite effective in a number of different contexts.

| Parameters | VGG | Convolution LSTM | 3D-CNN |
|---|---|---|---|
| *Proposed Model Parameterization* | | | |
| Learned Parameter Count | 31,232,865 | 41,125,543 | 2,210,530 |
| Training per-sample time (mean ± standard error) | 302 ± 0.97 ms | 802 ± 3.76 ms | 521 ± 3.21 ms |
| Size of a mini-batch | 240 | 240 | 240 |
| Rate of Dropout | 0.6 | NA | 0.6 |
| Epochs of training | 100 | 100 | 100 |
| Size of Batch | 4 | 4 | 4 |
| Normalization Input | True | False | True |
| Replications of the CV | 25 | 25 | 25 |

Table 1. Optimization parameters of neural networks

## 3. PROPOSED METHODOLOGY

### 3.1. Data gathering and imaging

Images for this study were acquired using a Thorlabs-made swept source optical coherence tomography (OCT) device. The system operated using a mode that did not require direct physical contact and which made use of a core wavelength of 1040 nm and a spectral bandwidth of 80 nm. Power was 0.36 mW, and 16 kHz was used for the axial scan rate, and the sample was scanned at 16 kHz. The strength of the stimulus given to the study population was quantified. The device featured an averaging process that combined four axial scans to enhance image quality. The tissue imaging system's axial resolution was 1 m while the transverse resolution was 11 m. These were really remarkable statistics. The overall imaging volume covered a spatial area of 4 mm x 4 mm laterally and extended to a depth of 2 mm. The obtained digital images had a width

of 750 pixels and a height of 752 pixels; each pixel took up about 5 micrometres in length and width. The image volume was exported as a collection of 2D images (or slices) before any further analysis or processing could be done on it.

The original purpose of collecting OCT data was to develop automatic segmentation algorithms [19] and perform 3D texture analysis [15]. In the end, this study accomplished both of its aims. If everything went as planned, the three-dimensional structure of an organ may be visualised by stitching together a series of OCT images along a third dimension. However, dealing with the fluctuating noise statistics that are created by optical backscattering is one of the most challenging elements of working with OCT data. These numbers could shift based on the underlying organ and, presumably, its health. Early attempts at quantitative analysis of optical coherence tomograms ran into difficulties due to variations in tissue density, optical absorption characteristics, and the concentration of scatterers [19]. Optical coherence tomography (OCT) is a noninvasive imaging modality for capturing anatomical detail in three dimensions. The OCT images had a Gaussian blur applied to them as part of the preprocessing phase to soften the sharp corners and reduce the overall effect of the abnormalities. However, as mentioned in Section 4.4, the neural network classifiers themselves took care of any additional calculations needed to account for the potential adverse effects of optical noise. This is an extremely important consideration. In order to automatically learn and extract significant properties from the OCT images, this method takes use of the capabilities of convolutional neural networks (CNNs). The analysis and categorization procedures improved as a result.

**3.2. Methodology based on a mouse**

The images used in this study were acquired by the research team using the TgMISIIR-TAg transgenic mouse strain. Female mice are able to develop spontaneous cases of bilateral epithelial ovarian cancer within the limitations of this paradigm [40, 41]. Epithelial ovarian cancer develops on both ovaries in every TAg+ TgMISIIR-TAg female mouse. By the time mice are eight weeks old, nearly all of them have developed invasive cancers within their ovaries. Most situations fit this description. In total, sixteen mice (eight TAg+ and eight wild-type) were sacrificed and scanned after 8 weeks of age for this investigation. The organs from these mice were surgically explanted and subsequently imaged using the optical coherence tomography (OCT) system.

It's essential to mention that the breeding protocol for these mice and the surgical explanation procedures are well-documented in previous publications [15, 19, 42]. Every scanned tissue sample was also subjected to a thorough inspection utilising immunohistochemistry and validated by a pathologist, ensuring the results are accurate and reliable. Finding out if tumours were present and their size was the primary goal of this examination. The presence or absence of TAg protein in cells was determined using morphological analysis. Ovarian cancer-like symptoms were observed in TAg+ mice as early as age eight, and this rigorous validation method confirmed this finding. Those interested in learning more about the histology analysis might look at a prior paper [43] by Sawyer and colleagues. The experimental design and data analysis for this study relies heavily on the work here.

**3.3. Preprocessing of Data**

The tomography imagery used in this study comprises images with dimensions of 750 pixels in width by 752 pixels in height as shown in Fig. 1, with pixel intensities ranging from 0 to 255. To make these images suitable for analysis by neural networks, we applied a series of preprocessing transformations. The preprocessing pipeline, depicted in Figure 1, outlines these operations.

First, we performed a linear rescaling of pixel intensities to bring them within the range [-1, 1]. This step is crucial for standardizing the data and ensuring that the neural network can effectively process it.

In the next step, we addressed the inherent speckle noise in the medium, which presents a difficulty because it might significantly hinder the efforts of automatic segmentation algorithms to distinguish ovarian tissue [44]. This was the critical point at which the issue was resolved. To make the images clearer and less noisy, we used a Gaussian filter on them all. The standard deviation of this Gaussian filter was set to 1, resulting in smoother images. Empirical evidence has shown that the Gaussian filter effectively reduces noise, especially in the context of the segmentation task studied in a prior work [46]. This approach was found to be more effective than alternatives such as median filtering, low-pass filtering, or anisotropic filtering.

Each image received a standardisation filter at the end of the preprocessing phase. Standardization was accomplished by selecting appropriate training data and then computing the mean and standard deviation of intensity on a pixel-by-pixel basis. Then, we subtracted the mean from each pixel's value and divided the resulting number by the empirical standard deviation. This normalization step ensures that the data have a consistent scale and distribution, which is beneficial for training neural networks. After this initial step of image preprocessing was complete for each patient, our cancer detection

strategy moved on to the training of a deep neural network. Classification of OCT image sequences was the task given to the neural network, which aided in the diagnosis of ovarian cancer.

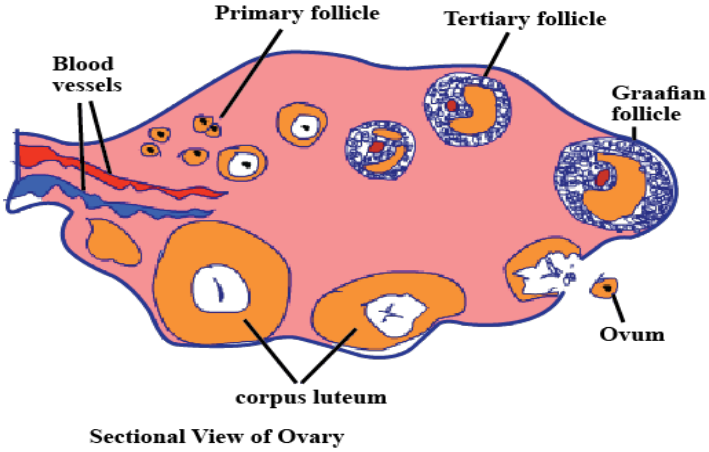


Figure 1. Sectional view of Ovarian Cancer

### 3.4. A Model for Classification

In the area of artificial neural networks, convolutional neural networks (CNNs) are proving to be increasingly popular. Synaptic connections between neurons and banks of neurons provide the basis of CNNs. These neurons compute their output states by convolving an input signal with filters learned during training. This process is akin to the way pixels in an image are processed, making CNNs particularly well-suited for computer vision tasks. Initially introduced to tackle handwritten digit classification, CNNs have since found widespread application in various computer vision domains.

The VGG architecture is a popular case of a convolutional neural network. Medical image analysis is only one of the many areas that can benefit from its unparalleled breadth and state-of-the-art performance in challenging image classification jobs. Convolutional layers (shown in yellow volumes) and pooling operations (used for downsampling via pixel aggregation) are two types of layers that make up the VGG model. Two spatial convolution layers in dimension two form the core of the convolutional block; these are followed by a max-pooling layer and provide sixty-four output channels. This process is repeated for each succeeding block, with more and more channels being added to the final product of each convolutional layer. To be more precise, each of the final two convolutional blocks produces 512 channels for the subsequent block.

The architecture of blocks 3–5 is consistent: it comprises of three convolutional layers wired in series. Layer 5 of a fully linked neural network, also called the re-encoding layer, and receives data from Block 5. This then links to a second completely connected layer called the decoding layer, which ultimately leads to a single neuron that is activated in a sigmoid pattern. Its unique architecture is very dissimilar to the traditional VGG implementation, which takes use of ReLU nonlinearities. Our model's convolutional layers are all trained with activation functions that are modified exponentials.

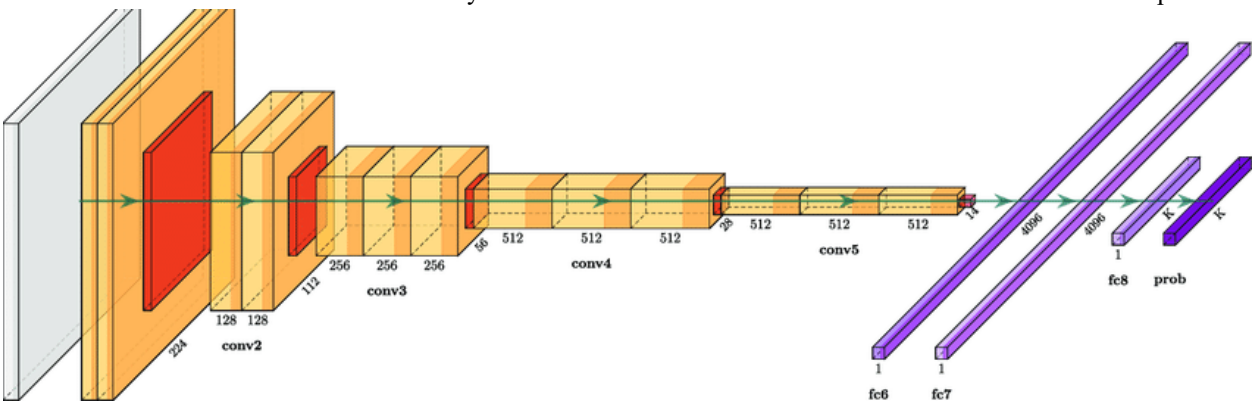


Figure 2. Architecture of pre-trained VGG network

For a given input sample, the decoder layer attempts to determine the probability that it belongs to each class (such as wild type or transgenic). Specifically, it uses logistic regression to analyse the OCT image's penultimate layer's encoding. For this reason, the model's categorization choice can be inferred from the decoding layer's output. This approach showcases the adaptability and robustness of CNNs, particularly when applied to complex image-based tasks.

The initialization of the VGG sub-network involves the use of weights that were previously learned on the Imagenet dataset, consisting of photographic images. This strategy leverages the concept of transfer learning [47], a common approach in many computer vision applications. Pre-training a deep neural network on a large dataset that is unrelated to the problem at hand, but which does contain a large amount of labelled data, is the first step in transfer learning. The network is then fine-tuned using the specific dataset that is relevant to the task at hand, after the first optimisation has been performed.

Specifically for our use case, the pre-trained VGG network provides useful feature maps, which are, in essence, nonlinear feature extractors learned from the Imagenet dataset. Once the network has been pre-trained using this broad set of data, we go on to the next stage, which involves fine-tuning it using the OCT (optical coherence tomography) information discussed previously. Despite the possibility of differences between the creation of natural scene imagery and biological tissue imaging (for example, melanoma dermoscopy compared to Imagenet), transfer learning has proven effective in a variety of neural network-based medical image tasks [45] and applications [48-50]. Our study implements VGG to reduce the cross-entropy between the probability distribution of the ground truth ($\{y_t\}_t$:¬ $p_y$ ) and the distributio n of decisions derived from the model's output $p_y$^ (implicitly conditioned on the data, $\{y_t\}$). To do this, we compare the model's decoded decision distribution to the probability distribution of the ground truth. This approach highlights the effectiveness of transfer learning in adapting pre-trained models to medical image analysis tasks, ultimately improving their performance and accuracy.

$$\varphi = \frac{1}{N} \sum_{i=1}^{N} [y_t \log \hat{y}_t + (1\text{-}y_t) \log (1\text{-}\hat{y}_t) \quad (1)$$

According to our model's framework, M represents the total number of photos in the training dataset. The used loss function, which was essentially a cross-entropy loss function $\varphi$, was employed. A conceptualization of this loss function is provided by the Kullback-Leibler (KL) divergence between two distributions, which may be determined empirically. Both the ground-truth distribution and the model's own forecast distribution have their own shapes and sizes. With this loss function, the goal is to minimise its value in order to have the model encode as much information as possible about its training dataset [51, 52]. In simpler terms, by minimizing the cross-entropy loss, the model aims to learn the patterns, relationships, and features within the training data that will enable it to make accurate predictions or classifications. This process is crucial in training neural networks and is a fundamental step in their ability to generalize and perform effectively on unseen data.

With the help of LSTM cells and their recurrent connections, which are governed by the LSTM cells themselves, Long Short-Term Memories (LSTMs) are a type of recurrent neural network designed to capture temporal associations within data [53]. This is because LSTMs rely on recurrent connections whose strength is determined by the activity of individual LSTM cells. However, recent advancements have introduced a novel class of convolutional neural networks incorporating feedback connections and gating mechanisms similar to those found in LSTMs. Applications ranging from weather prediction [54] to finding inconsistencies in video data [55] have demonstrated the potential of these innovative architectural concepts.

To take use of the 3D tomography data's natural spatial correlations and its ability to learn temporal relationships within its training data [56], we incorporate a convolutional LSTM into our system. We implement a convolutional LSTM, which draws upon prior work in the field for inspiration. The convolutional Long Short-Term Memory (LSTM) is shown in Figure 3. It uses max-pooling layers, and its input and convolutional blocks are both 2-channel, 2-dimensional spatial convolutions. These max-pooling layers downsample each channel in the same way as traditional CNNs does, halving the input resolution from its initial value [45]. Following that, the succeeding layers (shown in green) are constructed using 16-channel convolutional LSTMs. The dotted arrows represent the feedback links between the $g_t$ and ht layers. The intermediate states, g and h, are initialised to zero in the convolutional LSTM layers because to their strict adherence to the topologies [21].

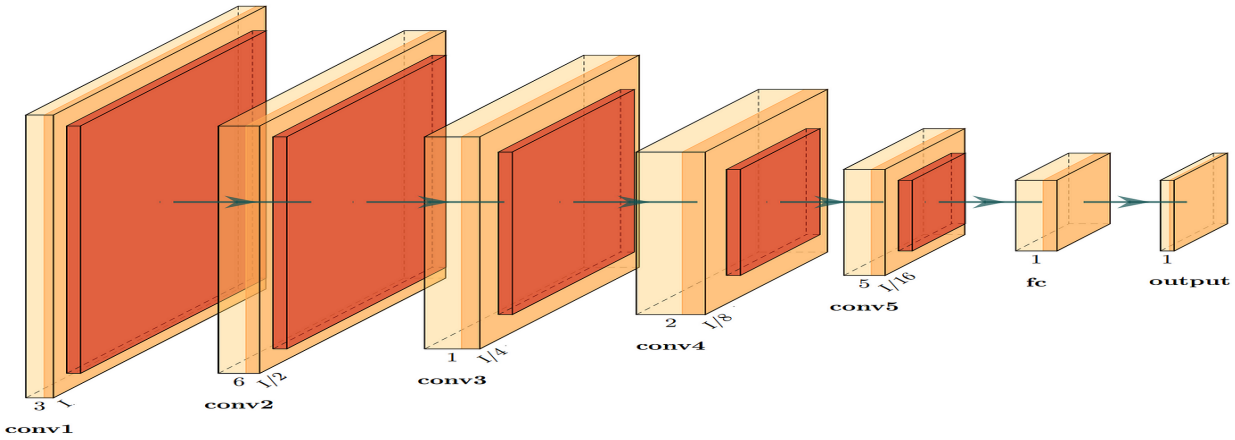


Figure 3. Architecture of convolutional LSTM Model

Then, the output from the h-th convolutional LSTM layer is fed into a chain of fully-connected feed-forward layers. To prepare h for the classification performed by the decoding layer, further encoding is added in these layers. In this model, every neuron except those in the output layer use sigmoid activation functions, which are a special form of activation that is only available in the recurrent neural network. To avoid any ambiguity, the rectified exponential linear activation function has been specified as...

$$\chi(y) = \begin{cases} exceptional(y) - 1, & y < 0, \\ y, & y \in [0,1] \\ 1, & y > 1 \end{cases} \quad (2)$$

This integration of convolutional LSTM layers enhances the model's ability to capture spatiotemporal relationships within the 3D tomography data, contributing to its effectiveness in tasks like medical image analysis and classification.

In our exploration of neural network models, we also considered the use of 3D Convolutional Neural Networks (3D CNNs), which represent an extension of traditional convolutional layers to accommodate spatial dimensions within imaging data. Applications ranging from the assessment of human stance [57] to the interpretation of medical imagery [58, 60] have demonstrated the efficacy of these three-dimensional convolutional neural networks (CNNs).

When compared to a 2D CNN, a 3D CNN differs primarily in the number of dimensions across which convolutions are performed. A 3D Convolutional Neural Network (CNN) is implemented in much the same way as a 2D CNN. In a 2D convolutional neural network (CNN), an image undergoes a single 2D convolution operation using a 2D kernel, which is the picture. A 3D convolutional neural network (CNN) filter, on the other hand, treats image sequences as if they were volumes and applies 3D kernels to them. To achieve this, sequential operations are performed on the photos. These 3D convolutional neural networks (CNNs) typically feature the following architecture of three distinct feed-forward subnetworks:

(a) A sequentially distributed 2D convolutional neural network (referred to as 'TimeDistributed' in TensorFlow terminology).

(b) The 3D CNN itself, where the third dimension arises from ordering elements within each sequence, denoted as y in $Y_t$.

Feed-forward layers employing yellow 2D spatial convolutions and feeding into orange max-pooling aggregation layers make up the main convolutional block in Figure 4. These layers are organised with 2, 4, and 8 channels (2D filters) in the first, second, and third convolutional layers, respectively. The brain of the network consists of a 64-channel 3D CNN coupled to a 4-channel 3D CNN. To signify these deeper levels, the colour green is used.

For classification by the decoding layer, shown in purple, the outputs of the 3D convolutional block are transmitted through a sequence of fully connected feed-forward layers, shown in turquoise. This is done repeatedly for each t-shaped "slice" of data. This architecture highlights the adaptability of 3D CNNs in handling volumetric data and their capacity to effectively learn and extract relevant features for classification tasks, such as identifying transgenic animals within the dataset.

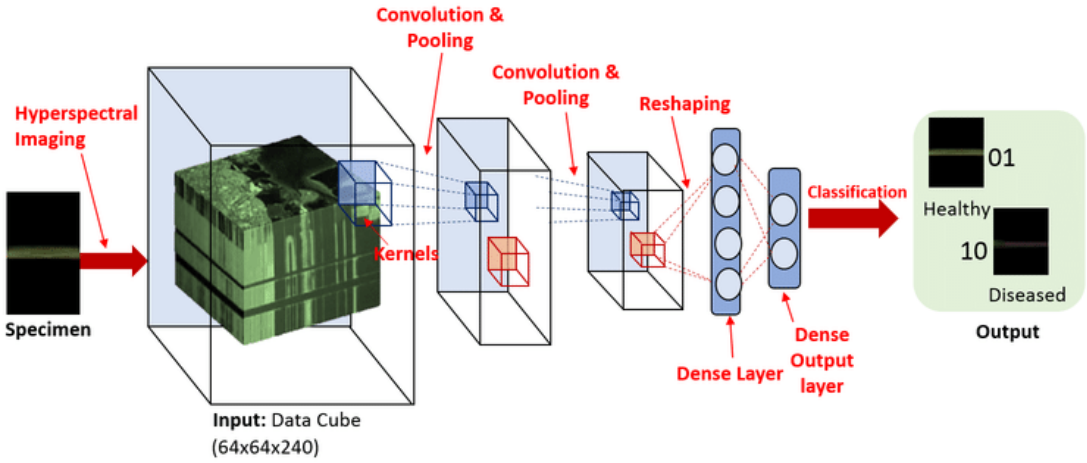


Figure 4. Architecture of 64-channel 3D CNN

## 4. RESULTS ANALYSIS

Three different types of neural networks—VGG, Convolutional LSTM, and 3D-CNN—are compared and contrasted based on the results of an empirical study. Our evaluation is conducted using the OCT (Optical Coherence Tomography) dataset as detailed in Section 4.1. When applied to the specific task of identifying cancer inside medical photos, these comparison analyses can offer insight on the benefits and drawbacks that are intrinsic to the performance of each algorithm. With this data, choices can be made with greater precision. The experimental design will be discussed first, followed by the findings and results themselves. In this summary, we present both the experimental paradigm and the many model parameterizations that we explored during the course of this research. This approach allows us to comprehensively assess and understand the performance of each neural network architecture and provides valuable insights into their suitability for the critical task of cancer detection within the context of OCT imaging data.

### 4.1 parameterizations of Model

In this subsection, we provide a detailed account of the various model parameterizations and configurations utilized in our study. These configurations are critical for understanding the nuances of each neural network's performance.

Our model's overall design is significantly bolstered by the use of dropout at the linkages from VGG to the re-encoding layer [61]. This dropout approach involves resetting the outputs of the VGG network's penultimate layer to zero in a random and dynamic fashion at various points throughout the training process. This randomly decreasing the outputs of neurons to zero during training serves multiple purposes: it reduces the training time required, it guides optimisation away from deep local minima in the loss function, and it ultimately enhances the model's generalisation.

Figure 2 shows that the input block includes the first two layers, whose weights and biases are fixed throughout training. This facilitates a more rapid training procedure while preserving previously learned characteristics. By reducing the total number of variable parameters, this technique efficiently shortens the training time. Most importantly, it has been observed that resetting these parameters to their optimum Imagenet settings has no appreciable negative effect on either the mean or maximum Area under the Curve (AUC) readings. We can learn a lot from this discovery. Figure 6 a, b shows a summary of the ROC curves, and when compared to Figure 5 (where all layer parameters are taken into account as variables during optimization), a small but non-negligible improvement in mean and peak AUC may be observed. If you look at the two numbers side by side, you can notice the difference.

To provide more uniformity throughout the optimization process, a penalty term is introduced to the loss function $\varphi$ (described in Equation 1). Weighted by a factor of 0.0005, this word represents the $L_2$ norm of the weights learned in the re-encoding layer. The 'Nadam' procedure [62], an extension of the extensively used Adam optimization method, is utilised to carry out the process of optimizing the model's weights and biases. The use of Nesterov momentum in the 'Nadam' algorithm increases the rate of convergence throughout the optimization process. To begin with, a learning rate of 0.001 is set, and it is dynamically adjusted according to the gradients of the loss function.

Importantly, we found that adding BN between the intermediate layers of our VGG implementation did not significantly affect the performance metrics that were evaluated for this study, in contrast to the 3D CNNs and convolutional LSTMs, which required BN to stabilize learning by normalizing the outputs of intermediate layers. This is a factor that needs to be

considered. This suggests that VGG's architecture, when combined with our specific dataset and parameterizations may not necessitate the use of BN for optimization and stability.

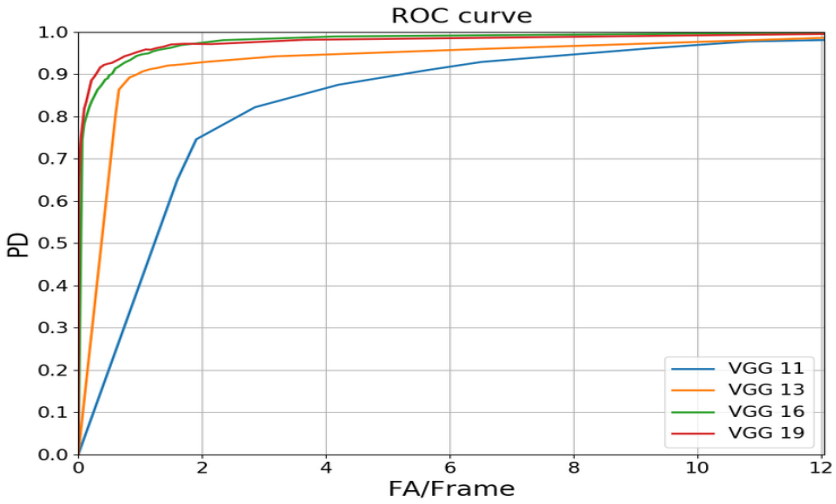


Figure 5. ROC curve for VGG network with different parameters

Unlike the 3D CNN and VGG-based models, our convolutional LSTM model can understand OCT (Optical Coherence Tomography) imagery directly without first undergoing the normalization process outlined in Section 4.3. That the data supplied into the convolutional LSTM model retains its natural characteristics without further preprocessing on the side of the user. However, both the VGG and 3D CNN-based models require normalized data in order to function.

Furthermore, we do not make use of dropout in the same way for our LSTM-based models during training as we do for our VGG- and 3D CNN-based models. Dropout is a technique commonly used to randomly deactivate neurons during training, which helps prevent over fitting and enhances model generalization.

The $L_2$ norm of the weights in each layer is used to regularize the cross-entropy loss, which is then used for optimization. This verifies the sincerity of the financial loss. Convolutional LSTMs require a different method of optimization than the VGG-based and 3D CNN models employed here. Convolutional LSTMs are optimized using the Adadelta approach [64]. Based on empirical analysis, this method was selected as the most stable and cost-effective option for this specific architecture and data collection.

In order to train the convolutional LSTM block, the inputs to the intermediate layers must be batch normalized. This occurs in the LSTM block after the convolutions have been performed. With this normalization method, we can more confidently estimate the loss function $\varphi$ gradients for the layers' corresponding parameters [63]. These gradients are estimated in a parameter-specific fashion. It has been found that the convolutional LSTM model benefits greatly from the addition of batch normalization because it accelerates learning and enhances performance in terms of generalization.

The initial learning rate for training is set at 0.001, and it is dynamically adjusted based on the gradients of the loss function $\varphi$, following the approach [64]. These considerations highlight the tailored parameterizations and optimization strategies employed for the convolutional LSTM model, taking into account the unique characteristics of the OCT imagery and the architecture's specific requirements for stable and effective training. As mentioned in Section 4.3, the 3D CNN model distinguishes out from the others proposed because its performance is enhanced by the normalization of OCT images. Because of this, the 3D CNN model stands out from the other proposed models. There is some evidence that this preprocessing step improves model performance when used with this data and architecture.

For the training of 3D CNNs, we apply a dropout rate of 50%. Dropout randomly deactivates neurons during training, aiding in preventing over fitting and enhancing the model's generalization. During model training, performance is improved by minimizing a loss function called the cross-entropy loss. Model weights' $L_2$ norm further regularizes this loss function. To fine-tune the 3D CNN's weights, we employ the Nadam algorithm [65], an extension of the Adam optimization approach with Nesterov momentum. The optimization process will reach a solution more quickly as a result of this.

Importantly, batch normalization (BN) is a critical component of the 3D CNN model. During training, it is applied to the inputs of the 3D convolutional block's intermediate layers. This normalization technique is crucial for ensuring steady estimation of gradients of the loss function $\varphi$ relative to these layers' parameters [63]. When BN is not applied to the inputs, the assessed 3D CNN models perform much worse.

As with the VGG-based models, the learning rate for the 3D CNNs is initially set to 0.001 and is dynamically adjusted during training based on gradients of the loss function $\varphi$. These specific parameterizations and strategies are tailored to the 3D CNN architecture and contribute to its ability to effectively learn and extract features from the OCT imagery.

**4.2 Experiment on Cross-validation**

The primary focus of our experiments centers on assessing the generalization performance of our models. Specifically, we are keen to understand how well these models can perform on data that they have never encountered during the training phase. For this purpose, we developed a leave-one-out cross-validation (CV) experiment, which is a robust method for assessing a model's ability to generalize to new data.

Using our leave-one-out CV design, we conduct experiments on each animal in our dataset. For every animal, we do one fold of the cross-validation test. The remaining 15 creatures are separated into the following sets within each fold:

1. A collection with only one member, which is the animal whose name is on the test subject's label.
2. Each of the seven groups had two animals: one wild-type and one transgenic.

Mini-batches representing each of the seven categorized subgroups are utilized to systematically train our models. The next mini-batch the model will be trained on will comprise entirely of validation subsets, it has been decided. This method reduces the impact of memory constraints while expanding the size of the batches used to evaluate the model against new data.

The validation set for the third and final mini-batch is based on the training data supplied in the first mini-batch. This is because validating data requires access to the original. An integral part of avoiding a phenomenon known as catastrophic forgetting is making sure models are tested on data they have never seen before throughout the training process. Catastrophic forgetting [66] occurs when fresh information causes a neural network to forget what it has already learned. As an additional precaution during training to avoid over fitting, we use early stopping. In machine learning, "early stopping" is pausing batch training when it's evident that extra training won't improve accuracy on the validation subset.

Each model receives a maximum of one positive and one negative sample per mini-batch during our regular training approach. After the training phase concludes, the model is tested on the reserved test data to determine how well it performed. This provides a thorough evaluation of the model's ability to generalize to novel data. This comprehensive experimental setup allows us to robustly measure the models' effectiveness in handling real-world scenarios where they encounter previously unobserved data.

**4.3 Results**

In Section 4.3, we noted that we use OCT (Optical Coherence Tomography) images from transgenic mice to test our models' prognostic abilities for predicting ovarian cancer incidence. Figure 6 displays the results of this test. Our goal in doing this research was to identify the most reliable of our models. The assessment of efficacy is conducted using Receiver Operating Characteristic (ROC) curves, a widely used tool in machine learning and medical diagnostics. On the ROC curve, the true positive rate (1-specificity) is plotted against the false positive rate (0-specificity).

In Figure 6a and b, the red dashed line depicts the results of a random forecast. The point at which the classifier's performance is no better than random guessing is indicated by this line. The most crucial measure of effectiveness is the AUC, or area under the ROC curve. This value approximates the likelihood that a given model will place a positive sample's likelihood higher than that of a randomly chosen negative sample. These numerical results are summarized for your convenience in Table 2.

Figure 6 depicts an interpolation of the mean ROC curves obtained during the cross-validation (CV) experiment described in Section 4.3. The highest AUC was achieved by the convolutional LSTM, but only by a marginal 0.089 over the 3D CNN (please refer to Table 2 for maximum and mean AUC values as well as standard error for these calculations). However, the VGG-based model's worst-case AUC was 0.89, significantly below the baseline. It should be noted that the VGG model required the longest training period of any of the models considered.

Interestingly, while the time costs of training a single epoch were similar for the 3D CNN and the convolutional LSTM, the VGG-based model took much more time. After putting these classifiers through their paces, this study discovered that convolutional LSTMs performed the best. These classifiers reached an AUC of 0.99, had a single false positive, and were error-free overall.

These findings point to the convolutional LSTM as a potentially game-changing method for detecting ovarian cancer in OCT images. Its strong performance, combined with efficient training times and low false positive rates, underscores its potential as a valuable tool in medical diagnostics for this specific application.

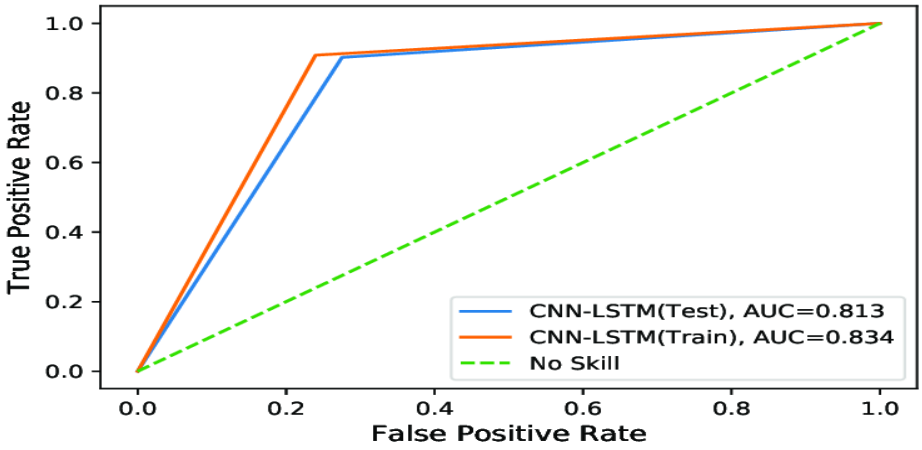


Figure 6(a). ROC – AUC of CNN LSTM Model

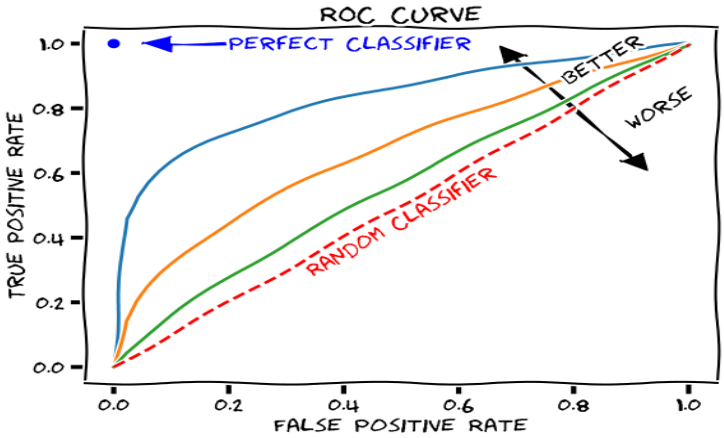


Figure 6(b). ROC – AUC of 3D-CNN Model

| Network Models | Final AUC | Average AUC ± Standard Error |
|---|---|---|
| ROC Curve Areas | | |
| Convolutional LSTM | 0.99 | 0.813 ± 0.042 |
| VGG | 0.89 | 0.61 ± 0.089 |
| 3D-CNN | 0.94 | 0.72 ± 0.032 |

Table 2. Cross validation experiment on final and average AUC achieved

## 5. CONCLUSION

These results are an essential first step in the direction of creating a fully automated OCT-based detection system for human ovarian cancer. The classifiers proposed in this study exhibit the capacity to autonomously learn and adapt abstract representations from tomographic data, enabling the detection of radiographic markers indicative of ovarian cancer within OCT imagery. Importantly, these classifiers accomplish this without the need for manual feature selection, which can be a time-consuming and labor-intensive process.

The results presented in this research demonstrate that, within the constraints of the dataset used, these classifiers achieve a high level of discrimination and are likely to generalize effectively to previously unseen data. It is also possible to reproduce their exceptional capability of making only a limited number of classification errors throughout several cycles of the leave-one-out cross-validation software. This robust performance highlights the potential of these models to serve as a foundation for the development of a powerful and reliable diagnostic system for ovarian cancer using OCT imagery.

To the best of the author's knowledge, this is the first study to present proof-of-concept using depth-resolved Optical Coherence Tomography (OCT) recordings of ovaries to identify malignancy. The data from this study were used to inform the development of this model. This is a notable achievement as ovarian tissue has proven to be a challenging medium for making genotype inferences are using both OCT and wide field fluorescence imaging techniques [67, 68–70].

Recent work on ovarian cancer detection using OCT employed a generalized linear model classifier. For the purpose of identifying cancerous ovarian tissue from healthy tissue, this approach has shown encouraging results [71]. Yet, as will be

discussed, there are important ways in which the current investigation differs from the prior attempt. Previous research focused on employing full-field OCT to image ovarian tissue biopsies; this classification method relied on features manually extracted from ovarian OCT data and was therefore subject to the limitations of human objectivity.

In contrast, the methodology presented in this research takes a distinct approach. Instead of relying on manually crafted features, our approach leverages machine learning techniques to automatically learn feature maps from the training data. In addition, we have used depth-resolved OCT measurements from healthy ovaries to validate our defined neural networks. This novel approach represents a significant advancement in the field, as it not only contributes to the development of an automated diagnostic system but also showcases the potential for depth-resolved OCT to address the challenging task of ovarian cancer detection.

**REFERENCES**

1. Rai, H.M., Yoo, J. A comprehensive analysis of recent advancements in cancer detection using machine learning and deep learning models for improved diagnostics. *J Cancer Res Clin Oncol* (2023).

2. Nguyen, K.T.P., Medjaher, K. & Tran, D.T. A review of artificial intelligence methods for engineering prognostics and health management with implementation guidelines. *Artif Intell Rev* **56**, 3659–3709 (2023).

3. Dhillon, A., Singh, A. & Bhalla, V.K. A Systematic Review on Biomarker Identification for Cancer Diagnosis and Prognosis in Multi-omics: From Computational Needs to Machine Learning and Deep Learning. *Arch Computat Methods Eng* **30**, 917–949 (2023).

4. 1. US Cancer Statistics Working Group, ‘‘US cancer statistics data visualizations tool, based on november 2018 submission data (1999-2016): US Department of Health and Human services, Centers for Disease Control and Prevention and National Cancer Institute,’’ Centers for Disease Control and Prevention and National Cancer Institute, 2019.

5. Abdolmanafi A, Duong L, Dahdah N, Cheriet F (2017) Deep feature learning for automatic tissue classification of coronary artery using optical coherence tomography. Biomed Opt Express 8(2):1203

6. Buys SS, Partridge E, Black A, Johnson CC, Lamerato L, Isaacs C, Reding DJ, Greenlee RT, Yokochi LA, Kessel B et al (2011) Effect of screening on ovarian cancer mortality: the prostate, lung, colorectal and ovarian (plco) cancer screening randomized controlled trial. Jama 305(22):2295–2303

7. Sawyer TW, Rice FF, Koevary JW, Connolly DC, Cai KQ, Barton JK (2019) In vivo multiphoton imaging of an ovarian cancer mouse model. Dis Breast Reprod Syst V 10856:1085605

8. Hee MR, Izatt JA, Swanson EA, Huang D, Schuman JS, Lin CP, Puliafito CA, Fujimoto JG (1995) Optical coherence tomography of the human retina. Arch Ophthalmol 113(3):325

9. Abra`moff M, Garvin MK, Sonka M (2010) Retinal imaging and image analysis. IEEE Rev Biomed Eng 1(3):169–208

10. Tsuboi M, Hayashi A, Ikeda N, Honda H, Kato Y, Ichinose S, Kato H (2005) Optical coherence tomography in the diagnosis of bronchial lesions. Lung Cancer 49(3):387–394

11. Otte S, Otte C, Schlaefer A, Wittig L, Hu¨ttmann G, Dromann D, Zeli A (2013) ‘‘OCT A-Scan based lung tumor tissue classification with Bidirectional Long Short Term Memory networks,’’ In 2013 IEEE International Workshop on Machine Learning for Signal Processing (MLSP), pp. 1–6

12. Sawyer TW, Chandra S, Rice PF, Koevary JW, Barton JK (2018) Three-dimensional texture analysis of optical coherence tomography images of ovarian tissue. Phys Med Biol 63(23):235020

13. Ferrante G, Presbitero P, Whitbourn R, Barlis P (2013) ‘‘Current applications of optical coherence tomography for coronary intervention’’

14. S. Xingjian, Z. Chen, H. Wang, D.-Y. Yeung, W.-K. Wong, and W.-c. Woo (2015) ‘‘Convolutional lstm network: A machine learning approach for precipitation nowcasting,’’ In Advances in neural information processing systems, 802–810

15. Gossage KW, Tkaczyk TS, Rodriguez JJ, Barton JK (2003) Texture analysis of optical coherence tomography images: feasibility for tissue classification. J Biomed Opt 8(3):570–575

16. Miller P, Astley S (1992) Classification of breast tissue by texture analysis. Image Vis Comput 10(5):277–282 17. Mostac¸o-Guidolin LB, Ko AC-T, Wang F, Xiang B, Hewko M, Tian G, Major A, Shiomi M, Sowa MG (2013) Collagen morphology and texture analysis: from statistics to classification. Sci Rep 3(1):2190

18. Ran AR, Tham CC, Chan PP, Cheng C-Y, Tham Y-C, Rim TH, Cheung CY (2020) ‘‘Deep learning in glaucoma with optical coherence tomography: a review,’’ Eye

19. Burgansky-Eliash Z, Wollstein G, Chu T, Ramsey JD, Glymour C, Noecker RJ, Ishikawa H, Schuman JS (2005) Optical coherence tomography machine learning classifiers for glaucoma detection: a preliminary study. Invest Ophthalmol Vis Sci 46(11):4147–52

20. Yanagihara RT, Lee CS, Ting DSW, Lee AY (2020) Methodological challenges of deep learning in optical coherence tomography for retinal diseases: a review. Trans Vision Sci Technol 9:11–2
21. Rahimy E (2018) Deep learning applications in ophthalmology. Current Opin Ophthalmol 29(3):254–260
22. Ditzler G, Bouaynaya N, Fathallah Shaykh HM (2019) Sparse kalman filtering for time-varying networks. BMC BioData Min 12:1–14
23. Ditzler G, Bouaynaya N, Shterenberg R (2018) AKRON: an algorithm for approximating sparse kernel reconstruction. Signal Process 144:265–270
24. Hariri LP, Liebmann ER, Marion SL, Hoyer PB, Davis JR, Brewer MA, Barton JK (2010) Simultaneous optical coherence tomography and laser induced fluorescence imaging in rat model of ovarian carcinogenesis. Cancer Biol Ther 10(5):438–447
25. Wang T (2015) An overview of optical coherence tomography for ovarian tissue imaging and characterization. Wiley Interdiscip Rev Nanomed Nanobiotechnol 7(1):1–16
26. Drexler W, Liu M, Kumar A, Kamali T, Unterhuber A, Leitgeb RA (2014) Optical coherence tomography today: speed, contrast, and multimodality. J Biomed Opt 19(7):071412
27. Schmitt J (1999) Optical Coherence Tomography (OCT): a review. IEEE J Sel Top Quantum Electron 5(4):1205–1215
28. Sawyer T, Chandra S, Rice P, Koevary J, Barton J (2018) Threedimensional texture analysis of optical coherence tomography images of ovarian tissue. Phys Med Biol 63:23
29. Welge WA, DeMarco AT, Watson JM, Rice PS, Barton JK, Kupinski MA (2014) Diagnostic potential of multimodal imaging of ovarian tissue using optical coherence tomography and secondharmonic generation microscopy. J Med Imag 1(2):025501
30. Brewer Ma, Utzinger U, Barton JK, Hoying JB, Kirkpatrick ND, Brands WR, Davis JR, Hunt K, Stevens SJ, Gmitro AF (2004) Imaging of the ovary. Technol Cancer Res Treat 3(6):617–627
31. Watanabe Y, Takakura K, Kurotani R, Abe H, Atanabe YUW, Akakura KEIT, Urotani REK (2015) Optical coherence tomography imaging for analysis of follicular development in ovarian tissue. App Opt 54(19):6111
32. Sawyer TW, Rice PF, Sawyer DM, Koevary JW, Barton JK (2018) Evaluation of segmentation algorithms for optical coherence tomography images of ovarian tissue. Diagn Treat Dis Breast Reprod Syst IV 10472:1047204 33. Alakwaa W, Nassef M, Badr A (2017) Lung cancer detection and classification with 3d convolutional neural network (3d-cnn). Lung Cancer 8(8):409
34. Johri A, Tripathi A (2019) et al., ‘‘Parkinson disease detection using deep neural networks,’’ In 2019 Twelfth International Conference on Contemporary Computing (IC3), pp. 1–4, IEEE
35. Yasir R, Rahman MA, Ahmed N (2014) ‘‘Dermatological disease detection using image processing and artificial neural network,’’ In 8th International Conference on Electrical and Computer Engineering, pp. 687–690, IEEE
36. Lee J, Prabhu D, Kolluru C, Gharaibeh Y, Zimin VN, Bezerra HG, Wilson DL (2019) Automated plaque characterization using deep learning on coronary intravascular optical coherence tomographic images. Biomed Opt Express 10:6497–6515, 11
37. Lee J, Prabhu D, Kolluru C, Gharaibeh Y, Zimin VN, Dallan LAP, Bezerra HG, Wilson DL (2020) Fully automated plaque characterization in intravascular OCT images using hybrid convolutional and lumen morphology features. Sci Rep 10:2596
38. He C, Li Z, Wang J, Huang Y, Yin Y, Li Z (2020) ‘‘Atherosclerotic Plaque Tissue Characterization: An OCT-Based Machine Learning Algorithm With ex vivo Validation ’’
39. Nour M, Co¨mert Z, Polat K (2020) A novel medical diagnosis model for covid-19 infection detection based on deep features and bayesian optimization. Appl Soft Comput 97:106580
40. Weiss K, Khoshgoftaar TM, Wang D (2016) A survey of transfer learning. J Big Data 3(1):1–40
41. Pan SJ, Yang Q (2010) A survey on transfer learning. IEEE Trans Knowl Data Eng 22(10):1345–1359
42. Russakovsky O, Deng J, Su H, Krause J, Satheesh S, Ma S, Huang Z, Karpathy A, Khosla A, Bernstein M, Berg AC, Fei-Fei L (2015) Imagenet large scale visual recognition challenge. Int J Comput Vision 115(3):211–252
43. Connolly DC, Bao R, Nikitin AY, Stephens KC, Poole TW, Hua X, Harris SS, Vanderhyden BC, Hamilton TC (2003) Female mice chimeric for expression of the simian virus 40 TAg under control of the MISIIR promoter develop epithelial ovarian cancer. Cancer Res. 63(6):1389–1397
44. Ahmed A, Yu K, Xu W, Gong Y, Xing E (2008) ‘‘Training hierarchical feed-forward visual recognition models using transfer learning from pseudo-tasks,’’ In European Conference on Computer Vision, pp. 69–82

45. Guo J, Liang Z, Scribner E, Ditzler G, Bouaynaya N, FathallahShaykh H (2018) ‘‘Nonlinear brain tumor model estimation with long short-term memory neural networks,’’ In IEEE/INNS International Joint Conference on Neural Networks
46. Zhang Z, Sabuncu M (2018) ‘‘Generalized cross entropy loss for training deep neural networks with noisy labels,’’ In Advances in neural information processing systems, pp. 8778–8788
47. Wang Y, Ma X, Chen Z, Luo Y, Yi J, Bailey J (2019) ‘‘Symmetric cross entropy for robust learning with noisy labels,’’ In Proceedings of the IEEE International Conference on Computer Vision, pp. 322–330
48. Gers FA, Schmidhuber J, Cummins F (1999) ‘‘Learning to forget: Continual prediction with lstm,’’ 1999 Ninth International Conference on Artificial Neural Networks ICANN 99. (Conf. Publ. No. 470)
49. Luo W, Liu W, Gao S (2017) ‘‘Remembering history with convolutional lstm for anomaly detection,’’ In 2017 IEEE International Conference on Multimedia and Expo (ICME), pp. 439–444, IEEE
50. Graves A, Ferna´ndez S, Schmidhuber J (2005) ‘‘Bidirectional lstm networks for improved phoneme classification and recognition,’’ In International Conference on Artificial Neural Networks, pp. 799–804, Springer
51. Clevert D-A, Unterthiner T, Hochreiter S (2015) ‘‘Fast and accurate deep network learning by exponential linear units (elus),’’ arXiv preprint arXiv:1511.07289
52. Mehta D, Rhodin H, Casas D, Fua P, Sotnychenko O, Xu W, Theobalt C (2017) ‘‘Monocular 3d human pose estimation in the wild using improved cnn supervision,’’ In 2017 international conference on 3D vision (3DV), pp. 506–516, IEEE
53. Ren X, Xiang L, Nie D, Shao Y, Zhang H, Shen D, Wang Q (2018) Interleaved 3d-cnn s for joint segmentation of small-volume structures in head and neck ct images. Med Phys 45(5):2063–2075
54. Navnath D. Kale, Dr. K. Raghava Rao, “Hybrid based cluster head selection for maximizing network lifetime and energy efficiency in WSN”, Journal of King Saudi University- Computer and Information Sciences (SCI Journal), April 2019.
55. Navnath D. Kale, Dr. K. Raghava Rao, “Maximizing network lifetime and energy efficiency of wireless sensor network using group search Ant lion with Levy flight”, IET Communication (SCI Journal), April 2020.
56. Quinn BA, Xiao F, Bickel L, Martin L, Hua X, Klein-Szanto A, Connolly DC (2010) Development of a syngeneic mouse model of epithelial ovarian cancer. J Ovarian Res 3(1):24
57. Watson JM, Rice PF, Marion SL, Bentley DL, Brewer MA, Utzinger U, Hoyer PB, Barton JK (2011) Multi-modality optical imaging of ovarian cancer in a post-menopausal mouse model. In: Advanced biomedical and clinical diagnostic systems IX, vol 7890. International Society for Optics and Photonics, p 78900W
58. Sawyer T, Koevary J, Rice F, Howard C, Austin O, Connolly D, Cai K, Barton J (2019) Quantification of multiphoton and fluorescence images of reproductive tissues from a mouse ovarian cancer model shows promise for early disease detection. J Biomed Opt 24(9):096010
59. LeCun Y, Bottou L, Bengio Y, Haffner P (1998) Gradient-based learning applied to document recognition. Proc IEEE 86(11):2278–2324.
60. Navnath Kale et. al., “CETR: CenterNet-Vision transformer model for wheat head detection”, Journal of Autonomous Intelligence (Scopus Journal), January 2024.
61. Navnath Kale et. al., “Design of Sensor Node for Drainage Blockage Monitoring System”, International Journal of Intelligent Systems and Applications in Engineering (Scopus Journal), August 2023.
62. Jaworek-Korjakowska J, Kleczek P, Gorgon M (2019) ‘‘Melanoma thickness prediction based on convolutional neural network with vgg-19 model transfer learning,’’ In Proceedings of the IEEE Conference on Computer Vision and Pattern Recognition Workshops, pp. 0–0
63. Simonyan K, Zisserman A (2014) ‘‘Very deep convolutional networks for large-scale image recognition,’’ arXiv preprint arXiv:1409.1556
64. Deng J, Dong W, Socher R, Li L-J, Li K, Fei-Fei L (2009) ‘‘Imagenet: A large-scale hierarchical image database,’’ In 2009 IEEE conference on computer vision and pattern recognition, pp. 248–255, Ieee
65. Xiang EW, Cao B, Hu DH, Yang Q (2010) Bridging domains using world wide knowledge for transfer learning. IEEE Trans Knowl Data Eng 22(6):770–783
66. Pan S, Tsang I, Kwok J, Yang Q (2011) Domain adaptation via transfer component analysis. IEEE Trans Neural Netw 22(2):199–210
67. Navnath Kale et. al., “Computer Vision and Its Intelligence in Industry 4.0”, Machine Learning Techniques and Industry Applications (Scopus indexed book chapter), April 2024.

68. Navnath Kale et. al., “Analyzing electroencephalogram signals with machine learning to comprehend online learning media”, Indonesian Journal of Electrical Engineering and Computer Science, 2024, 35(3), pp. 1876–1885.
69. Navnath Kale et. al., “Revolutionizing Wireless Networks: Cutting-edge Machine Learning Paradigms for Next Generation Connectivity”, Nanotechnology Perceptions, 2024, 20(S6), pp. 785–796.
70. Schweikert G, Widmer C, Scho¨lkopf B, Ra¨tsch G (2008) An empirical analysis of domain adaptation algorithms for genomic sequence analysis. In: NIPS, vol 8. Citeseer, pp 1433–1440
71. Srivastava N, Hinton G, Krizhevsky A, Sutskever I, Salakhutdinov R (2014) Dropout: a simple way to prevent neural networks from overfitting. J Mach Learn Res 15(1):1929–1958
72. Dozat T (2016) ‘‘Incorporating nesterov momentum into adam,’’ International Conference on Learning Representations (ICLR)
73. Santurkar S, Tsipras D, Ilyas A, Madry A (2018) ‘‘How does batch normalization help optimization,’’ In Advances in Neural Information Processing Systems, pp. 2483–2493
74. Zeile MD (2012) ‘‘Adadelta: an adaptive learning rate method,’’ arXiv preprint arXiv:1212.5701
75. Ruder S (2016) ‘‘An overview of gradient descent optimization algorithms,’’ arXiv preprint arXiv:1609.04747 76. Grossberg S (1988) Nonlinear neural networks: principles, mechanisms, and architectures. Neural Netw 1(1):17–61
77. Fawcett T (2006) An introduction to ROC analysis. Pattern Recognit Lett 27:861–874
78. Sawyer TW, Koevary JW, Howard CC, Austin OJ, Rice PF, Hutchens GV, Chambers SK, Connolly DC, Barton JK (2020) Fluorescence and multiphoton imaging for tissue characterization of a model of postmenopausal ovarian cancer. Lasers Surg Med 52(10):993–1009